

Resynchronization of islanded unbalanced ADNs: Control, synchrocheck and experimental validation

Sherif Fahmy^{a,*}, Quentin Walger^b, Mario Paolone^a

^a Distributed Electrical Systems Laboratory, École Polytechnique Fédérale de Lausanne, EPFL, Lausanne, Switzerland

^b R&D Systems, Leclanché, Yverdon-les-bains, Switzerland

ARTICLE INFO

Keywords:

Active distribution networks
Island resynchronization
Synchronism check
Unbalanced three-phase control

ABSTRACT

The problem of securely reconnecting active distribution networks (ADNs) – e.g. microgrids – to their upstream grids at the point of common coupling (PCC) has been extensively discussed by the existing literature. The latter is commonly referred to as *resynchronization* and has to be done with care in order to avoid large transient current flows resulting from differences of nodal voltage phasors at both sides of the PCC. The active resynchronization process can be split into two tasks: the PCC-control and the synchrocheck. The PCC-control refers to the process used to steer the PCC nodal voltage at the ADN's side (i.e. downstream) towards the PCC nodal voltage at the upstream-grid's side (i.e. upstream). The synchrocheck refers to the algorithm used to check the synchronization (i.e. phasor alignment within tolerances) of the upstream and downstream PCC nodal voltages. Methods for PCC-control and synchrocheck presented in the literature commonly ignore the ADN's operational constraints and rely on the assumption of a balanced system. In this respect, the contribution of this paper is twofold. First, an approximated optimal-power-flow is proposed to control ADNs' resources in order to rapidly steer their PCC downstream nodal voltages close to their non-controllable upstream counterparts. Second, an Interpolated-Discrete-Fourier-Transform (IpDFT)-based synchrocheck that verifies the alignment of all three-phases of both upstream and downstream nodal voltages at the PCC, is proposed. The algorithms associated to both contributions are experimentally validated on the CIGRE-low-voltage-benchmark-microgrid at the Distributed Electrical Systems Laboratory (DESL) at the École Polytechnique Fédérale de Lausanne (EPFL) where the results of the developed synchrocheck are further benchmarked against the Schneider Electric's Micom P143 grid relay.

1. Introduction

Active distribution networks (ADNs), e.g. microgrids, are small power grids for electricity distribution hosting dispersed power generation, demand-side management and energy storage devices. ADNs can be controlled and operated in either grid-connected-mode, i.e. connected to an upstream network at the point of common coupling (PCC), or islanded-mode, i.e. disconnected from the upstream network. The latter configuration represents a solution to guarantee the continuity of supply when the upstream network is experiencing faults or outages that may propagate downstream [1]. In practice, a reconnection to the upstream-grid is inevitable due to lack of supply and/or sufficient energy storage. The transition between the two modes must be handled carefully. In particular, during a resynchronization process (i.e. islanded to grid-connected), it is important to ensure that the three-phase nodal voltages on both sides (i.e. upstream and downstream) of the PCC are within security bounds in terms of magnitude, phase-angle and

frequency, before closing the breaker (i.e. ensure nodal voltage phasors synchronization and alignment) [2]. Failing in doing so may provoke large current transients that can damage the ADN's equipments.

As explained in the IEEE std. on distributed resource island systems (e.g. islanded ADNs) [1], the resynchronization process can be done in three ways: *open-transition*, *passive* and *active*. Open-transition resynchronization refers to the complete denenergization of the ADN before reclosing the PCC breaker. Passive resynchronization relies on constantly checking the alignment of the upstream and downstream PCC nodal voltages and only closing the breaker if they are synchronized, without the need to denenergize the local – i.e. downstream – grid. The algorithm used to detect the PCC nodal voltages synchronization is referred to as *synchronism-check* or *synchrocheck* and its function is “the determination that acceptable voltages exist on the two sides of the circuit breaker, and the phase-angle and frequency difference (slip) between them is within a specified limit for a specified time.” (cf. [3] for

* Corresponding author.

E-mail addresses: sherif.fahmy@epfl.ch (S. Fahmy), quentin.walger@leclanche.com (Q. Walger), mario.paolone@epfl.ch (M. Paolone).

Nomenclature

ADN	Active Distribution Network
ADN-CC	Active Distribution Network Central Controller — proposed PCC-control
BLSA	Backtracking Line Search Algorithm
CCB	Controllable Circuit Breaker
CMS	Centralized Monitoring System
CPC	Controllable Power Converters
DG	Distributed Generator
e-IpDFT	Enhanced Interpolated Discrete Fourier Transform
FCL	Frequency Control Law
IpDFT	Interpolated Discrete Fourier Transform
OP	Optimization Problem
OPF	Optimal-Power-Flow
PCC	Point of Common Coupling
PCC-Control	Control mechanism that actively steers the PCC downstream three-phase-nodal-voltages to synchronize with the upstream counterparts
PID	Proportional Integral Derivative
PLL	Phasor-Locked-Loop
PMU	Phasor Measurement Units
SB	Synchro-Breaker
SC	Sensitivity Coefficient
SYNCHRO	Proposed Synchrocheck Algorithm

details on when this functionality is needed and how it is configured). Active resynchronization, which is the process of interest in this work, refers to frameworks with a control mechanism that actively steers the PCC downstream nodal voltages in order to synchronize it with their upstream counterparts. The latter control mechanism is hereinafter referred to as *PCC-control*.

In the literature, methods tackling the problem of *PCC-control* can be clustered in two categories: *single* and *multiple* device-based frameworks.

Single device methods rely on having a specific device connected in close proximity to the PCC aiming to locally control the downstream PCC nodal voltages. Traditionally that device was a synchronous-generator-based-resource whose speed (i.e. frequency) and nodal voltage magnitude could be controlled, respectively, through their governor and automatic-voltage-regulators. For instance, in [4], a dedicated distributed generator (DG) is proposed to be installed in order to locally align the nodal voltage phase-angles and frequencies at both sides of the PCC. Another example is in [5] where authors propose to control the DG through an adaptive-droop-control-strategy to adjust the frequency, phase-angle and amplitude of the downstream PCC nodal voltages. Alternatively, non-generator-based-dedicated devices used for the resynchronization process were also proposed in the literature. For instance, in [6], authors suggest to connect a controllable capacitor-bank near the PCC in order to locally change the downstream nodal voltages through reactive-power compensation. Even though such solutions relying on one physical device may work well, the fact that ADNs are not expected to resynchronize frequently, renders this solution costly as *most* dedicated devices may remain idle in long non-resynchronization periods.

Multiple device methods rely on controlling one or more resources already present in the ADN in order to steer the PCC downstream nodal voltages. In [7] authors present a Proportional-Integral-Derivative (PID)-based method where a central controller generates set-points for DGs that are assumed to be controlled using their respective

droops. In [8] authors present a distributed synchronization strategy relying on PID-based transfer function control. To ensure better post-resynchronization behavior they consider the ADN's voltage unbalances by extending the typical criteria listed in [2] to include harmonics and nodal voltage negative-sequence limitations. In [9], a distributed PI-controller-based method is proposed where DGs cooperatively communicate with each other to adjust their local droops in order to collectively steer the downstream PCC nodal voltages towards their upstream counterparts. Similarly in [10], authors present a distributed consensus-based phase-angle droop-method for DGs to perform PCC-control. Additionally, it leverages the use of phasor measurement units (PMUs) to get accurate measurements of the phase-angle of different nodal voltages.

In most of the above works the *synchrocheck* functionality is implemented through phasor-locked-loop (PLL)-based algorithms that measure both nodal voltage phase-angles and frequencies in conjunction with standard magnitude measurements. In the specific literature on *synchrocheck* most works do the same, however, some present alternative methods. For instance, in [11], the authors present a method leveraging low-pass filters, voltage zero-crossing detection coupled with a digitizer to measure nodal voltage magnitudes, phases and frequencies, then actuate a breaker in case of synchronism. More recently, data driven approaches have been proposed. For instance, in [12], a learning-based classification method is proposed to detect phasor synchronization. Alternatively, in [13], a method is proposed to detect phasor alignment by comparing the correlations of the different analog nodal voltage signals over several periods.

In all the above *PCC-control* frameworks, authors ignore the downstream-ADN's operational, i.e. static and power quality constraints, i.e. branch currents magnitudes, nodal voltages magnitudes, ratios of nodal voltages negative-over positive-sequences and zero-over positive-sequences, all within predefined bounds. Furthermore, none of these works explicitly use PMU measurements to detect the synchronization of both upstream and downstream PCC nodal voltage phasors. Indeed, some use PMUs in order to get accurate measurements of nodal voltage phase-angles but it remains unclear whether PMUs are directly used in the *synchronism-check*. As a result, this paper proposes: (i) a centralized optimal-power-flow (OPF)-based algorithm to control an ADN's resources to steer the PCC downstream nodal voltages towards their upstream non-controllable counterparts, and (ii) an Interpolated-Discrete-Fourier-Transform (IpDFT)-based synchrocheck method that checks the alignment of all three-phases of both upstream and downstream nodal voltages at the PCC. Both contributions are experimentally validated – i.e. an active resynchronization using both contribution was achieved within 1–2 s – on the CIGRE low-voltage benchmark microgrid available at the Distributed Electrical Systems Laboratory (DESL) at the École Polytechnique Fédérale de Lausanne (EPFL), referred to as EPFL-DESL microgrid, where the results of the developed synchrocheck are further benchmarked against the Schneider Electric's Easergy Micom P143 grid relay [14].

The rest of the paper is structured as follows. Section 2 schematically presents an overview of the paper's contributions. Section 3 contains the details of the proposed PCC-control strategy. Section 4 presents the proposed synchrocheck algorithm. Section 5 first presents the experimental setup, then, shows the experimental validation results of both proposed contributions. Section 6, finally, concludes the paper.

2. Resynchronization overview

As discussed in the IEEE std. for ADN controllers [15], the reconnection of an ADN to its upstream network requires the four steps reported in Table 1. The proposed active resynchronization framework deals with steps 1 and 2 of Table 1 while also trying to guarantee smoothness and minimal effort for the fulfillment of steps 3 and 4. Fig. 1 schematically illustrates the contributions of this paper.

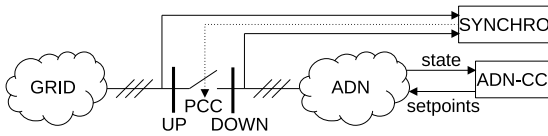


Fig. 1. Resynchronization schematic overview.

Table 1
Reconnection steps proposed by the IEEE std. for ADN controllers [15].

Steps	Action
1 - Initiation	Match PCC nodal voltage phasors within prescribed limits
2 - Returning	Set local controllers and protection devices through appropriate setpoints
3 - Grid-connected	Close PCC-breaker to reconnect
4 - Normal operation	Transition to grid-connected control and restore non-critical loads

The first contribution is the ADN-central controller (ADN-CC) that aims at steering, over several control timesteps, the downstream nodal voltages at the PCC towards their upstream target counterparts while accounting for the ADN's operational, i.e. static and power-quality, constraints. This entails that the ADN is protected pre- and post-reconnection as invasive actions, e.g. non-essential load-shedding that will need to be restored post-resynchronization, are implicitly minimized. Therefore, the PCC-control algorithm running on the ADN-CC deals with steps 1 & 2 of Table 1, but also minimizes said-restorations of step 4. As seen in Fig. 1, the ADN-CC needs as an input the ADN's-state, provided, for instance, by a centralized monitoring system (CMS), and, outputs setpoints for the ADN's controllable resources (cf. Section 3).

The second contribution, denoted as SYNCHRO, consists of a synchrocheck running an IpDFT-based method that extracts the per-phase phase-angle, frequency and magnitude of both PCC nodal voltage phasors then compares them, vis-a-vis the tolerances presented in [2], to verify and claim synchronization (cf. Section 4). As seen in Fig. 1, the SYNCHRO block needs as inputs all six nodal voltages at both sides (i.e. DOWN and UP) of the PCC. Its output is a boolean signal guaranteeing the synchronization of the PCC phasors. The output can be directly coupled with breaker-actuation signals (see Section 5.2).

3. PCC-control

As previously mentioned, the proposed PCC-control strategy is an OPF that is approximately-solved using a gradient-descent-based algorithm. The idea of the proposed algorithm is to *quickly* and *securely* steer the PCC downstream nodal voltages over several timesteps. In the following, first an overview of the control framework is given, second, the problem formulation is detailed, and, finally the algorithm used to solve the problem is presented.

3.1. Control framework: Assumptions and overview

In this work, we consider that distributed energy resources (i.e. loads, sources and storage) in an ADN can be regulated by means of controllable power converters (CPCs). Furthermore, we only consider two control-modes for CPCs: i. *grid-forming* mode where the converter's ADN-side-nodal-voltage magnitude and frequency are regulated, and, ii. *grid-following* mode where the converter's ADN-side-nodal-active-and-reactive-power injections are regulated. As a result, no rotating machines are present in the considered ADNs. Additionally, in the adopted control framework, as long as the ADN is islanded, only one CPC is assumed to be controlled in grid-forming mode. This entails that the latter plays the role of the slack bus since it sets the voltage

at its bus and the frequency of the ADN.¹ Naturally, this implies that it must be connected to a bidirectional resource able to respond to power imbalances and compensate grid-losses (e.g. energy storage device [16]). It is important to note that, the unique slack assumption is not strict as the proposed PCC-control strategy can easily be extended to multi-slack islanded ADNs by accounting for the slacks grid-forming CPCs' power-sharing-law in the problem constraints (cf. Section 3.2.5 for considered constraints) and by ensuring that the latter all implement the same frequency set-point.

Next, we assume that the ADN's grid topology, line-parameters and compound admittance matrix are known² and that its state (i.e. nodal voltage phasors at every bus), including the upstream³ PCC bus, is available in real-time by means of a PMU-aided state-estimation⁴ algorithm running on the CMS. The deployed state estimator is assumed to output estimates with at least the same accuracy as the minimum measurement requirements found in the IEEE std. for interconnecting distributed resources with electrical power systems [2]. Furthermore, the use of a state-estimator increases reliability as they are inherently built for redundancy and bad-data rejection, e.g. the state can be accurately estimated even if 20%–30% of the input measurements are lost or erroneous. The CMS communicates – with a high reporting rate of, e.g., 20ms – the state to the ADN-CC, which is the device running the PCC-control algorithm that computes explicit set-points to be implemented by the CPCs. If that communication is broken, or if the CMS fails to compute the grid state, the ADN-CC halts its control actions. The control period of the ADN-CC is chosen to be short enough (e.g., 100ms) such that the downstream nodal voltages at the PCC are steered towards their upstream targets after a few control-steps even if the set-points computed at each control-step are sub-optimal (cf. Section 3.3). Note that, the fast reporting rates and control-periods, given as examples above, correspond to the ones of the setup used for the experimental validation (cf. Section 5.1). However, if these numbers increase due to practical limitations, the proposed methods would still be applicable.

Finally, we consider that each CPC is managed by a dedicated agent (real-time controller) that communicates with the ADN-CC. The ADN-CC sends explicit set-points to be implemented and, oppositely, the CPC's agent advertises the measured active and reactive nodal power injections as well as the updated power limits of the resource it is connected to (e.g. the maximum discharge power of a battery decreases with its state-of-charge). Fig. 2 shows an overview of the adopted PCC-control framework, as presented above.

3.2. Problem formulation

3.2.1. Grid model

In this paper, we consider three-phase⁵ ADNs with any grid topologies, i.e. meshed or radial, and $|\mathcal{N}|$ nodes, where \mathcal{N} is the set of all

¹ We assume that the frequency is the same everywhere in the ADN, which is reasonable given the small size of distribution grids.

² This assumption is only needed for the method used for the considered grid model linearizations (cf. Section 3.2.3). However, as explained in [17], other *model-less* techniques exist in the literature and can achieve similar linearization performance accuracies without the knowledge of the grid-model.

³ There are no particular assumptions made on the upstream PCC nodal voltages, however, the state of grounding of both upstream and downstream networks needs to be identical and, naturally, all measurement devices used in the process of inducing the states need to have the same references.

⁴ This assumption is considered to (i) match the setup (cf. Section 5.1) used to perform the experimental validation, and, (ii) achieve high-controlling speeds enabled by the accuracy and high-reporting rates of PMUs. However, it is important to note that, other forms of *slower* state-estimators can be used to feed the states to the proposed PCC-control algorithm forcing it to adapt the rapidness of its control decisions but ultimately reach its intended target.

⁵ Phases are denoted by superscripts a, b and c .

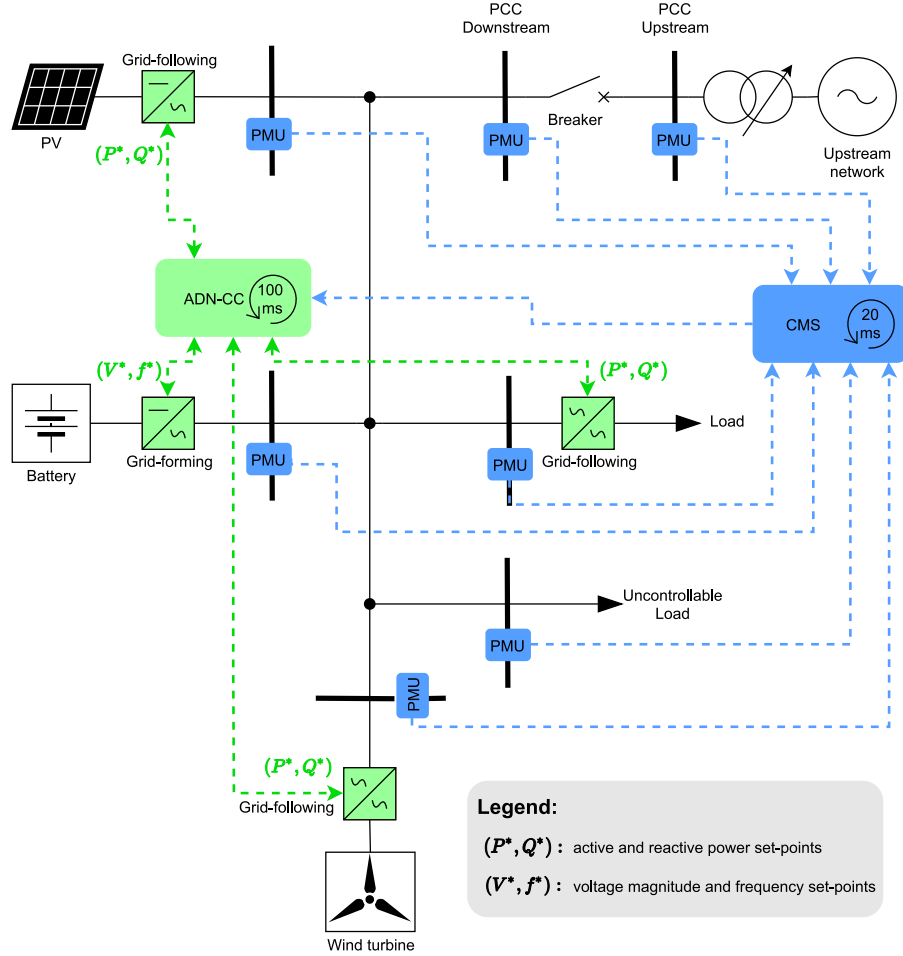


Fig. 2. Schematic illustration of the propose PCC-control framework for the resynchronization of islanded ADNs using explicit set-points.

nodes. \mathcal{PQ} is the set of both zero-injection nodes and nodes where uncontrollable resources are connected. \mathcal{K} is the set of PQ-nodes where CPCs in grid-following mode are connected. $S = \{s\}$ is the set containing the slack node (i.e. the node to which is connected the only considered CPC in grid-forming mode when the ADN is islanded). Without loss of generality,⁶ we assume that $\mathcal{PQ} \cap \mathcal{K} \cap S = \emptyset$ and $|\mathcal{PQ}| + |\mathcal{K}| + |S| = |\mathcal{N}|$. The set of all electrical branches is denoted by $\mathcal{L} = \{(i, j) \mid i, j \in \mathcal{N}, \bar{Y}_{ij} \neq \mathbf{O}\}$, with $\bar{Y}_{ij} = [\bar{Y}_{ij}^{\phi\psi}] \in \mathbb{C}^{3 \times 3}$ being the submatrices composing the compound-block-admittance matrix \bar{Y} [18].

Finally, the power flow equations, i.e., the relation between the nodal phase-to-ground voltages $\bar{E}_i = [\bar{E}_i^a, \bar{E}_i^b, \bar{E}_i^c]$ and the nodal apparent power injections $\bar{S}_i = [\bar{S}_i^a, \bar{S}_i^b, \bar{S}_i^c]$ are given by⁷

$$\bar{S}_i = P_i + jQ_i = \bar{E}_i \circ \sum_{j \in \mathcal{N}} \underline{Y}_{ij} \bar{E}_j \quad \forall i \in \mathcal{N} \quad (1)$$

3.2.2. Voltage-dependent loads

In this paper, we model the active and reactive nodal power absorptions of voltage-dependent loads using the generalized model presented

⁶ Virtual branches (i.e. close-to-lossless) and buses could be added in case different-mode CPCs or resources share the same node.

⁷ The operator \circ denotes the Hadamard product and \underline{z} denotes the complex conjugate of the complex number $\bar{z} = |\bar{z}| \angle(\bar{z})$.

in [17], namely,

$$\begin{cases} P_i^\phi = P_{i,n} \sum_{(\alpha,\lambda) \in \Lambda_i^\phi} \alpha |\bar{E}_i^\phi|^\lambda \\ Q_i^\phi = Q_{i,n} \sum_{(\zeta,\omega) \in \Omega_i^\phi} \zeta |\bar{E}_i^\phi|^\omega \end{cases} \quad (2)$$

where, for phase ϕ of node i , $P_{i,n}^\phi$ and $Q_{i,n}^\phi$ denote the reference active and reactive nodal power injections at nominal voltage. Λ_i^ϕ and Ω_i^ϕ are sets containing weights and exponents. Some examples of weights and exponents together with their identification methods can be found in [19].

3.2.3. Linearization of the grid model

In order to achieve a convex OPF that can be solved in real-time, the power-flow equations are linearized around the estimated states provided by the CMS. The linearization of the power flow Eqs. (1) including (2), is made possible through the computation of *sensitivity coefficients* (SCs), namely the partial derivatives of electrical quantities (e.g. nodal voltages, branch currents, nodal sequence voltages, slack apparent power) with respect to control variables, which are in our case, the active-and-reactive-nodal-power-injection-set-points for grid-following converters and the nodal-voltage-magnitude-and-frequency-set-points for the grid-forming converter. The derivation of the SCs uses the method presented in [17], which enables the computation

of the magnitude and phase-angle SCs as well. By leveraging a first-order Taylor expansion, the variations of electrical quantities can be estimated using SCs that are computed using the system's present state (denoted thereafter with the subscript 0). Note that, even though the control time-step is short (e.g., 100 ms), the ADN-CC steers the ADN's global state slowly enough such that the use of phasors and, consequently, SCs are adequate to formulate the constraints of the optimization problem (see Section 3.2.5). Finally, since the islanded-ADN's operating frequency is constrained within a tight range (e.g., ± 0.6 Hz) around 50 Hz, we assume that its contribution to the variations of other electrical quantities (e.g. nodal voltage magnitudes) can be neglected without loss of accuracy; hence, the SCs involving the frequency as a control variable are ignored.

3.2.4. Power converters' dynamics

The implementation of a new control set-point by a CPC is not done instantaneously due to the latter's dynamics. Let us denote by Δx^* the desired variation of the control set-point sent to a CPC at the beginning of the control step, and by Δx the actual implemented variation at the end of the control step, that is, after the control period ΔT . Thus, we can write without loss of generality

$$\Delta x(t = \Delta T) = \beta(t = \Delta T) \Delta x^* \quad (3)$$

where $\beta(t)$ is a function that tends to 0 as the control period is shortened and tends to 1 when the latter gets sufficiently long compared to the CPC's time-constant (e.g. slew-rate). The control period being a fixed parameter, we assume that the gain β is known a-priori and is, therefore, constant for each control variable. This is acceptable for all control variables except the frequency as its dynamics are needed for the estimation of the downstream phase-angles at the PCC. Indeed, the latter is based on the integral of the frequency, hence, the function accounting for the frequency evolution during some prediction horizon ΔT_h must be known. In this respect, we model the frequency dynamics of the CPC in grid-forming mode as a first-order transfer function, with a step response given by

$$\Delta f(t) = H(t - L) (1 - e^{-r(t-L)}) \Delta f^* \quad (4)$$

where $H(t)$ is the Heaviside function, L is the converter's delay and r its slew rate. Consequently, at the end of the prediction horizon, the angle variation due to the frequency evolution is:

$$\begin{aligned} \int_0^{\Delta T_h} 2\pi f(t) dt &= \int_0^{\Delta T_h} 2\pi (f_0 + \Delta f(t)) dt \\ &= 2\pi f_0 \Delta T_h + \beta_f \Delta f^* \\ \text{with } \beta_f &= 2\pi \left(\Delta T_h - L - \frac{1 - e^{-r(\Delta T_h - L)}}{r} \right) \end{aligned} \quad (5)$$

3.2.5. Full optimization problem

In this section, we formulate the PCC-control problem in the form of a constrained convex optimization problem. For the sake of readability, we adopt the notation $|\mathbf{z}| = z$ where \mathbf{z} is the vector of moduli of the complex vector $\mathbf{z} \in \mathbb{C}^n$, $n \geq 1$. By leveraging on first-order Taylor expansions, we consider implicitly the relation between an approximated quantity $\mathbf{x} \in \mathbb{R}^n$ (or $\bar{\mathbf{x}} \in \mathbb{C}^n$), $n \geq 1$, and its variation $\Delta \mathbf{x}$ ($\Delta \bar{\mathbf{x}}$) from its initial centroid \mathbf{x}_0 ($\bar{\mathbf{x}}_0$), that is, $\mathbf{x} = \mathbf{x}_0 + \Delta \mathbf{x}$ ($\bar{\mathbf{x}} = \bar{\mathbf{x}}_0 + \Delta \bar{\mathbf{x}}$). The optimization problem (OP) OP1, is given by

$$\begin{aligned} \text{OP1: } \min_{\substack{\Delta P_k^*, \Delta Q_k^* \\ \Delta E_s^*, \Delta f^*}} & \| \mathbf{E}_{dwn} - \mathbf{E}_{up,0} \|^2 + \gamma \| \theta_{dwn} - \theta_{up} \|^2 \\ \text{subject to} & \end{aligned}$$

$$\mathbf{E}_{i,min} \leq \mathbf{E}_i \leq \mathbf{E}_{i,max} \quad \forall i \in \mathcal{N} \setminus S \quad (6a)$$

$$\mathbf{I}_{ij} \leq \mathbf{I}_{ij,max} \quad \forall (i, j) \in \mathcal{L} \quad (6b)$$

$$\mathbf{S}_s \leq \mathbf{S}_{s,max} \quad s \in S \quad (6c)$$

$$\mathbf{P}_{s,min} \leq \mathbf{P}_s \leq \mathbf{P}_{s,max} \quad s \in S \quad (6d)$$

$$\mathbf{Q}_{s,min} \leq \mathbf{Q}_s \leq \mathbf{Q}_{s,max} \quad s \in S \quad (6e)$$

$$\mathbf{E}_i^{zero} \leq \text{tol}_{zero} \mathbf{E}_i^{pos} \quad \forall i \in \mathcal{N} \setminus S \quad (6f)$$

$$\mathbf{E}_i^{neg} \leq \text{tol}_{neg} \mathbf{E}_i^{pos} \quad \forall i \in \mathcal{N} \setminus S \quad (6g)$$

$$\left(\mathbf{P}_k^{\phi,*} \right)^2 + \left(\mathbf{Q}_k^{\phi,*} \right)^2 \leq \left(\mathbf{S}_{k,max}^{\phi} \right)^2 \quad \forall k \in \mathcal{K} \quad (6h)$$

$$\mathbf{P}_{k,min} \leq \mathbf{P}_k^* \leq \mathbf{P}_{k,max} \quad \forall k \in \mathcal{K} \quad (6i)$$

$$\mathbf{Q}_{k,min} \leq \mathbf{Q}_k^* \leq \mathbf{Q}_{k,max} \quad \forall k \in \mathcal{K} \quad (6j)$$

$$\mathbf{E}_{s,min} \leq \mathbf{E}_s^* \leq \mathbf{E}_{s,max} \quad s \in S \quad (6k)$$

$$f_{min} \leq f^* \leq f_{max} \quad (6l)$$

$$\Delta \mathbf{E}_i = \sum_{k \in \mathcal{K}} \left(\mathbf{C}_{P_k}^{E_i} \Delta \mathbf{P}_k^* + \mathbf{C}_{Q_k}^{E_i} \Delta \mathbf{Q}_k^* \right) + \mathbf{C}_{E_s}^{E_i} \Delta \mathbf{E}_s^* \quad (6m)$$

$$\Delta \mathbf{I}_{ij} = \sum_{k \in \mathcal{K}} \left(\mathbf{C}_{P_k}^{I_{ij}} \Delta \mathbf{P}_k^* + \mathbf{C}_{Q_k}^{I_{ij}} \Delta \mathbf{Q}_k^* \right) + \mathbf{C}_{E_s}^{I_{ij}} \Delta \mathbf{E}_s^* \quad (6n)$$

$$\Delta \mathbf{S}_s = \sum_{k \in \mathcal{K}} \left(\mathbf{C}_{P_k}^{S_s} \Delta \mathbf{P}_k^* + \mathbf{C}_{Q_k}^{S_s} \Delta \mathbf{Q}_k^* \right) + \mathbf{C}_{E_s}^{S_s} \Delta \mathbf{E}_s^* \quad (6o)$$

$$\Delta \bar{\mathbf{S}}_s = \sum_{k \in \mathcal{K}} \left(\bar{\mathbf{C}}_{P_k}^{S_s} \Delta \mathbf{P}_k^* + \bar{\mathbf{C}}_{Q_k}^{S_s} \Delta \mathbf{Q}_k^* \right) + \bar{\mathbf{C}}_{E_s}^{S_s} \Delta \mathbf{E}_s^* \quad (6p)$$

$$\Delta \mathbf{E}_i^{seq} = \sum_{k \in \mathcal{K}} \left(\mathbf{D}_{P_k}^{E_i} \Delta \mathbf{P}_k^* + \mathbf{D}_{Q_k}^{E_i} \Delta \mathbf{Q}_k^* \right) + \mathbf{D}_{E_s}^{E_i} \Delta \mathbf{E}_s^* \quad (6q)$$

$$\Delta \boldsymbol{\varphi} = \sum_{k \in \mathcal{K}} \left(\mathbf{C}_{P_k}^{\boldsymbol{\varphi}} \Delta \mathbf{P}_k^* + \mathbf{C}_{Q_k}^{\boldsymbol{\varphi}} \Delta \mathbf{Q}_k^* \right) + \mathbf{C}_{E_s}^{\boldsymbol{\varphi}} \Delta \mathbf{E}_s^* \quad (6r)$$

$$\Delta \theta_{dwn} = (2\pi f_0 \Delta T_h + \beta_f \Delta f^*) \mathbf{e} + \Delta \boldsymbol{\varphi} \quad (6s)$$

$$\Delta \theta_{up} = (2\pi f_{up,0} \Delta T_h) \mathbf{e} \quad (6t)$$

The objective function of OP1 is the weighted sum of the ℓ^2 -norms of the deviations between the upstream (\cdot_{up}) and downstream (\cdot_{dwn}) PCC nodal voltage magnitudes and phase-angles. The tuning parameter $\gamma \in \mathbb{R}$ ensures that both objective terms are comparable (i.e. are of the same nature) enabling it to give more importance either to the nodal voltage magnitude or phase-angle realignment. Note that, the frequency deviation is not explicitly minimized because it is already accounted for in the phase-angle objective term. Indeed, the phase-angle being the integral of the frequency, if the former is resynchronized continuously for multiple timesteps, then the latter is necessarily resynchronized as well. Therefore, this requires to compute the integrals of the ADN's and upstream frequencies over a prediction horizon that is longer than the control period, i.e. $\Delta T_h > \Delta T$. Additionally, the frequency control law resulting from the resolution of OP1 would be aggressive if $\Delta T_h = \Delta T$ as the PCC nodal-voltage phase-angles would be forced to be synced at the end of the short, e.g. 100 ms, ΔT which may lead to large setpoint oscillations between subsequent control timesteps.

The optimization variables are the variations of the active and reactive power set-points $\Delta \mathbf{P}_k^*$, $\Delta \mathbf{Q}_k^*$ for CPCs in grid-following mode $k \in \mathcal{K}$, and the variations of the voltage magnitude and frequency set-points $\Delta \mathbf{E}_s^*$, Δf^* for the CPC in grid-forming mode.

Constraints (6a) to (6e) guarantee the static constraints, namely, that the nodal voltage magnitudes $\mathbf{E}_i = [\mathbf{E}_i^a, \mathbf{E}_i^b, \mathbf{E}_i^c]$, $\forall i \in \mathcal{N} \setminus S$, branch-current magnitudes⁸ $\mathbf{I}_{ij} = [\mathbf{I}_{ij}^a, \mathbf{I}_{ij}^b, \mathbf{I}_{ij}^c]$, $\forall (i, j) \in \mathcal{L}$ and slack nodal power injections $\bar{\mathbf{S}}_s = \mathbf{P}_s + j\mathbf{Q}_s = [\bar{\mathbf{S}}_s^a, \bar{\mathbf{S}}_s^b, \bar{\mathbf{S}}_s^c]$ are within bounds.

Constraints (6f) and (6g) guarantee the power quality constraints by enforcing nodal voltage grid balance to be within the bounds stated in [20]. Let the vector of voltage sequence components be defined as $\bar{\mathbf{E}}_i^{seq} = [\bar{\mathbf{E}}_i^{zero}, \bar{\mathbf{E}}_i^{pos}, \bar{\mathbf{E}}_i^{neg}]$, \mathbf{E}_i^{zero} denotes the zero-sequence nodal voltage magnitude, \mathbf{E}_i^{pos} the positive-sequence nodal voltage magnitude and \mathbf{E}_i^{neg} the negative-sequence nodal voltage magnitude, of node i .

⁸ For more information about the computation of branch-currents and their associated SCs refer to [17].

The parameters $tol_{zero}, tol_{neg} \in \mathbb{R}_+$ define, respectively, the maximum acceptable magnitudes of zero- and negative-sequence nodal voltages with respect to the positive-sequence (cf. [20]).

Constraints (6h) to (6j) ensure that the active and reactive power setpoints respect the power limits – in terms of active, reactive and apparent powers – of all CPCs in grid-following mode. Similarly, constraints (6k) and (6l) ensure that the voltage magnitude and frequency setpoints given to the CPC in grid-forming mode comply with the converter's and ADN devices' operating limits.

The linearized model of the grid is described by constraints (6m) to (6r), which are first-order Taylor expansions of grid-quantities around centroids inferred from the states provided by the CMS. As previously explained, the expansions leverage the use of SCs. To simplify notation, the SCs and the dynamics of the power converters (cf. Section 3.2.4) are encapsulated in the matrices $C_x^y, D_x^y \in \mathbb{R}^{3 \times 3}$ and $\bar{C}_x^y \in \mathbb{C}^{3 \times 3}$. More specifically, the latter are defined as

$$C_x^y = \left[\frac{\partial y^\phi}{\partial x^\psi} \right]_0 \beta_{k \text{ or } s}^w, \quad y \in \{E_i, I_{ij}, S_s, \varphi\}$$

$$\bar{C}_x^y = \left[\frac{\partial \bar{y}^\phi}{\partial x^\psi} \right]_0 \beta_{k \text{ or } s}^w, \quad \bar{y} = \bar{S}_s$$

$$D_x^y = \left[\frac{\partial y^\sigma}{\partial x^\psi} \right]_0 \beta_{k \text{ or } s}^w, \quad y = E_i, \forall \sigma \in \{zero, pos, neg\}$$

where $\phi, \psi \in \{a, b, c\}$, $x \in \{P_k^*, Q_k^*, E_s^*\}$, $k \in \mathcal{K}$, $s \in S$.

Finally, constraints⁹ (6s) and (6t) describe, respectively, the evolution of the phase-angles (i.e. phases a, b & c) at the downstream (θ_{dwn}) and the upstream (θ_{up}) sides of the PCC. The variations of the downstream PCC nodal voltage phase-angles depend on: (i) the integral of the ADN's frequency during the prediction horizon which is given by (5) and (ii) control set-points variations other than the frequency (i.e. ΔP_k^* , ΔQ_k^* , and ΔE_s^*) which are given by (6r) where $\Delta\varphi \in \mathbb{R}^3$. Unlike the downstream case, the model of the upstream grid is assumed to be unknown. As a result, the frequency of the upstream network is considered constant between control timesteps, which means that the variation of the upstream PCC nodal voltage phase-angles θ_{up} during the prediction horizon (ΔT_h) is computed as the integral of the upstream frequency estimate provided by the CMS.

3.2.6. Decoupling the full optimization problem

Even though OP1 can be solved in real-time, we propose to go one step further by splitting the downstream PCC nodal voltage magnitudes steering and phase-angles/frequency regulation. The reason behind this is that in OP1 the only constraint where the frequency intervenes with other control variables is (6s), namely the variation of the downstream PCC nodal voltage phase-angles. In practice, in ADNs with low-power rating devices, a change in frequency will have more effect on nodal voltage phase-angles compared to variations of any other control variables (i.e. nodal active and reactive power injections for PQ-nodes and nodal voltage magnitudes for slack-nodes). Thus, if control setpoints variations other than the frequency do not lead to big downstream-PCC-nodal-voltage-phase-angles' variations, i.e. $\Delta\varphi^\phi \ll \beta_f \Delta f^*$, $\forall \phi \in \{a, b, c\}$, OP1 can be reduced to only steer the downstream PCC-nodal-voltage-magnitudes, i.e. all variables and constraints related to the frequency and downstream-PCC-nodal-voltage-phase-angles can be removed from the optimization problem. As a result, the objective is reduced to $\|E_{PCC} - E_{up,0}\|^2$ and constraints (6l), (6r), (6s) and (6t) can be removed. Thus leading to the optimization problem OP2, given by,

$$\text{OP2: } \min_{\substack{\Delta P_k^*, \Delta Q_k^*, \\ \Delta E_s^*}} \|E_{dwn} - E_{up,0}\|^2$$

⁹ The symbol e denotes the three-dimensional vector of ones, that is, $e = [1, 1, 1]$.

subject to

$$(6a), (6b), (6c), (6d), (6e), (6f), (6g), (6h), (6i), (6j), (6k), (6m), (6n), (6o), (6p), (6q)$$

In parallel to solving OP2, a control law regulating the frequency (FCL2) and, therefore, the nodal voltage phase-angles at the downstream-side of the PCC needs to be derived. We propose an analytical control-law. More specifically, the idea is to equate the downstream phase-angles with the upstream phase-angles at the end of the prediction horizon (ΔT_h), in other words, the control-law computes the optimal downstream ADN frequency setpoint that would guarantee nodal voltage phase-angles' alignment at both sides of the PCC after the prediction horizon. Starting from

$$\theta_{dwn,0} + \int_0^{\Delta T_h} 2\pi f(t)dt = \theta_{up,0} + \int_0^{\Delta T_h} 2\pi f_{up}(t)dt, \quad (7)$$

one can write, using (5) and – as previously explained – assuming that the upstream frequency remains constant during the prediction horizon,

$$\theta_{dwn,0} + 2\pi f_0 \Delta T_h + \beta_f \Delta f^* = \theta_{up,0} + 2\pi f_{up,0} \Delta T_h, \quad (8)$$

from which we isolate the frequency set-point variation Δf^* – that will be sent to the CPC in grid-forming mode – leading to (9).

$$\Delta f^* = \frac{\theta_{up,0} - \theta_{dwn,0} + 2\pi(f_{up,0} - f_0)\Delta T_h}{\beta_f} \quad (9)$$

Finally, in order to guarantee constraint (6l) of the non-decoupled problem, the proposed decoupled frequency control-law, i.e. FCL2, outputs a coerced set-point f^* . FCL2 is given by (10).

$$\text{FCL2 : } f^* = \begin{cases} f_{min} & \text{if } f_0 + \Delta f^* < f_{min} \\ f_{max} & \text{if } f_0 + \Delta f^* > f_{max} \\ f_0 + \Delta f^* & \text{otherwise} \end{cases} \quad (10)$$

3.3. Optimization problem resolution

As previously explained, thanks to the high update rate of the ADN-CC, computing sub-optimal set-points at each control step is acceptable as it would still succeed at steering, over time, the PCC downstream nodal voltages towards their upstream counterparts (i.e. it does not need to necessarily achieve full-resynchronization in one control step). Thus, solving the convex optimization problem by computing gradient-descent-iterates that converge towards the optimum in a few control timesteps is perfectly fine. In this respect, we propose to solve the optimization problems (i.e. OP1 and OP2) using a projected-gradient-descent-algorithm coupled with a barrier-method. To illustrate how the gradient descent operates, let us consider the following generic-form-optimization-problem:

$$\begin{aligned} \min_x \quad & g_0(\mathbf{x}) \\ \text{s.t.} \quad & g_i(\mathbf{x}) \leq 0, \quad i = 1, \dots, m \\ & \mathbf{Ax} = \mathbf{b} \end{aligned}$$

where, in our case, \mathbf{x} is the vector of control set-points variations (i.e. $[\Delta P_k^*, \Delta Q_k^*, \Delta E_s^*, \Delta f^*]$ for OP1 and $[\Delta P_k^*, \Delta Q_k^*, \Delta E_s^*]$ for OP2, $\forall k \in \mathcal{K}$ and $s \in S$), $g_0(\mathbf{x})$ is the objective function, $g_{1\dots m}(\mathbf{x})$ are the inequality constraints (i.e. (6a) to (6l) for OP1 and (6a) to (6k) for OP2) and $\mathbf{Ax} = \mathbf{b}$ the linear equality constraints (i.e. (6m) to (6t) for OP1 and (6m) to (6q) for OP2). As suggested in [21], to approximately solve the problem, the constrained problem is first relaxed into an unconstrained one. Namely, the inequality constraints ($g_i(\mathbf{x}) \leq 0$) are included in the objective function ($g_0(\mathbf{x})$) by means of logarithmic barriers $c_i(\mathbf{x}) = -\log(-g_i(\mathbf{x}))$, $\forall i = 1, \dots, m$ and the linear equality constraints ($\mathbf{Ax} = \mathbf{b}$) are injected into $g_0(\mathbf{x})$ and each $c_i(\mathbf{x})$ by means of direct substitution. This leads to,

$$\min_x \quad g_0(\mathbf{x}) + \frac{1}{u} \sum_{i=1}^m c_i(\mathbf{x})$$

where the parameter $u > 0$ tunes the trade-off between optimality and feasibility. The unconstrained optimization problem can be solved using the barrier method as presented in [21]. The barrier method consists in solving a sequence of subproblems, called *centering steps*, while varying u . Each centering step is composed of several gradient steps. For each gradient step, the step-size is chosen by means of backtracking line search.¹⁰ Indeed, each centering step yields a sequence of iterates $\{\mathbf{x}^{(1)}, \mathbf{x}^{(2)}, \dots, \mathbf{x}^{(k)}, \dots\}$ called a *central path*. The last element of every central path is called the *central point*. The subsequent centering step starts at the previous-iteration's central point considering a new objective for the unconstrained optimization problem where u is increased by a factor $\mu > 0$, hence putting more weight on optimality. The first starting point of the first centering and gradient steps is set to $\mathbf{0}$.

In addition to the barrier method, the vector of set-points variations is projected onto the feasible set, $\Gamma = \{\mathbf{x} | g_i(\mathbf{x}) \leq 0, \forall i = 1, \dots, m\}$, at the end of each gradient step. The projection is done to: (i) ensure the *strict* feasibility of each iterate in case some constraints $g_i \leq 0$ are not strictly ensured by the barrier method, and (ii) make sure that the subsequent gradient descent step starts from a feasible point. A Euclidean projection onto the feasible set is computationally as complex as solving the original optimization problems (i.e. OP1 and OP2). As a result, the Euclidean projection is approximated by the method of alternating projections [22], denoted by $\tilde{\Pi}_\Gamma(\mathbf{x})$, that is, the projection of \mathbf{x} onto the feasible set Γ . Note that, each inequality constraint of the optimization problems OP1 and OP2 defines either a half-space or a disc. Hence, the application of the method of alternating projections to both problems only requires the computation of orthogonal projections onto hyperplanes and circles, which can be done analytically.

The proposed method, coupling the barrier method and the method of alternating projections, to solve the generic-form-optimization-problem is presented in Alg 1. The parameters n_c and n_g denote the number of centering and gradient steps, respectively. The parameter u_0 is the initial trade-off between optimality and feasibility. We propose to set it to:

$$u_0 = \eta \frac{\|\sum_{i=1}^m \nabla c_i(\mathbf{x}^{(0)})\|}{\|\nabla g_0(\mathbf{x}^{(0)})\|}, \quad 0 < \eta < 1$$

meaning that during the first centering step, feasibility is preferred to optimality, thus steering the first central point near the analytic center of the feasible set.

3.4. PCC-control synthesis and scalability

To summarize, two methods are proposed to steer the downstream-PCC-nodal-voltage phasors towards their upstream counterparts. The first relies on approximately solving OP1 using Alg. 1 and is applicable to ADNs with high-power-rated CPCs in grid-following mode that can induce nodal-voltage-phase-angle variations comparable to ones resulting from frequency variations. The second relies on using FCL2 together with the approximate solving of OP2 using Alg. 1 and is applicable to ADNs where the induced nodal-voltage-phase-angle variations due to set-point-changes at CPCs in grid-following mode are *negligible* compared to ones following frequency changes. Indeed, for a generic ADN, *a-priori* load-flow computations should be done to determine which method is best-suited.

Concerning the scalability of the proposed methods, as the grid size increases – e.g. larger number of power grids' nodes and more controllable resources – there are three aspects to consider:

¹⁰ Given the complexity of OP1 and OP2, an exact line-search is not used to compute the optimal step-size for each gradient-step. For more information about inexact and exact line-search algorithms see [21].

Algorithm 1 Proposed gradient descent method

Inputs: $\mathbf{x}^{(0)} = \mathbf{0}$, g_0 , $c_{1,\dots,m}$, $\Gamma := \bigcap_{i=1}^m g_i$

Parameters: n_c , n_g , $u = u_0$, μ

```

for  $j = 0$  to  $n_c - 1$  do                                # Loop of centering steps
  for  $k = 0$  to  $n_g - 1$  do                                # Loop of gradient steps
    Compute  $\nabla g_0(\mathbf{x}^{(k)})$ 
    Compute  $\nabla c_i(\mathbf{x}^{(k)})$ ,  $i = 1, \dots, m$ 
     $\nabla h(\mathbf{x}^{(k)}) \leftarrow \nabla g_0(\mathbf{x}^{(k)}) + \frac{1}{u} \sum_{i=1}^m \nabla c_i(\mathbf{x}^{(k)})$ 
    Compute step size  $\alpha^{(k)}$  using backtracking line search in the
    direction of  $-\nabla h(\mathbf{x}^{(k)})$ 
     $\mathbf{y}^{(k+1)} \leftarrow \mathbf{x}^{(k)} - \alpha^{(k)} \nabla h(\mathbf{x}^{(k)})$ 
     $\mathbf{x}^{(k+1)} \leftarrow \tilde{\Pi}_\Gamma(\mathbf{y}^{(k+1)})$                 # Analytical alternating projs
  end for
   $\mathbf{x}^{(0)} \leftarrow \mathbf{x}^{(n_g)}$ 
   $u \leftarrow \mu u$ 
end for

```

Output: $\mathbf{x}^{(n_g)}$

- (1) *Minor delays in the construction of optimization problem objective and constraints*¹¹;
- (2) *Minor delays in the execution of Alg. 1.*
- (3) *No delays in the state-estimator and subsequent sending of the state to the ADN-CC:* The state estimator problem remains linear and can be solved efficiently.

The first two aspects entail possible *minor* delays in steering the downstream-PCC-nodal-voltages towards their upstream counterparts as the ADN-CC is forced to have longer control timesteps.

4. Synchrocheck

As previously mentioned, the proposed synchrocheck strategy relies on an IpDFT-based method that extracts the per-phase nodal voltage phasor of both-sides of the PCC then checks whether their differences are within the tolerances given in [2]. If the tolerances are successively respected for a given amount of time, the phasors are deemed synchronized and the PCC breaker can be closed (i.e. the process of reconnecting the ADN to its upstream-grid is green-lighted). In the following, first the IpDFT-based method for phasor estimation is presented, then, an algorithmic formulation of the full synchrocheck algorithm of the SYNCHRO block (see Fig. 1) is presented.

4.1. IpDFT-based phasor extraction

The IpDFT-based phasor extraction used in this work is the enhanced-IpDFT (e-IPDFT) method presented in [23]. In the following, we briefly summarize the basics of e-IPDFT. Assuming that an electrical quantity (\hat{I}_p) can be modeled in time by a main tone varying around a rated frequency f_{rate} (i.e. neglecting harmonics, DC offsets and amplitude and/or phase modulations) and is sampled, e.g. by a PMU, with a frequency $f_{sam} = 1/t_{sam}$ over a time window $T_{win} (= D \times t_{sam})$, where D is the number of samples per sampling period t_{sam} short-enough to assume stationarity, one can write

$$\hat{I}_p(d) = I_p \cos(2d\pi f_p t_{sam} + \phi_p), \quad d \in [0, D - 1] \quad (11)$$

¹¹ For more information on the scalability of the computation of the different SCs refer to [17].

where l_p , f_p and ϕ_p are the amplitude, frequency and phase-angle of the main-tone that will be estimated. Following the assumptions in [23] and assuming the use of the Hanning windowing function with a window sequence $\{w(d)\}$, the DFT of (11) can be written as,

$$\hat{L}_p(m) = \frac{1}{W} \sum_{d=0}^{D-1} w(d) \cdot \hat{l}_p(d) \cdot e^{-jm\kappa_d}, \quad m \in [0, D-1] \quad (12)$$

where $W = \sum_{d=0}^{D-1} w(d)$ and $\kappa_d = 2\pi d/D$. Following the assumptions in [23], the true frequency f_p is situated between two successive DFT bins and can be expressed, as a function of the DFT frequency resolution $1/T_{win}$, as

$$f_p(\delta) = \frac{m_1 + \delta}{T_{win}} \quad (13)$$

with $-0.5 < \delta \leq 0.5$ being the deviation of f_p from the frequency with the maximum DFT bin (i.e. $m_1 T_{win}$). From there, as explained in [23], with $\psi = \text{sign}(|\hat{L}_p(m_1 + 1)| - |\hat{L}_p(m_1 - 1)|)$, one can directly write,

$$l_p(\delta) = 2|\hat{L}_p(m_1)| \cdot \frac{\pi\delta \cdot (1 - \delta^2)}{\sin(\pi\delta)} \quad (14)$$

$$\phi_p(\delta) = \angle(\hat{L}_p(m_1)) - \pi\delta$$

where

$$\delta = \psi \frac{2|\hat{L}_p(m_1 + \psi)| - |\hat{L}_p(m_1)|}{|\hat{L}_p(m_1 + \psi)| + |\hat{L}_p(m_1)|} \quad (15)$$

As explained in [23], from this point, one can go a step further by trying to remove the spectral interference due to the negative image of the DFT spectrum from the positive bins-used-in (14). To do so, first, the DFT of (11) is re-expressed as,

$$\hat{L}_p(m) = \frac{1}{W} [\bar{V}_p(\delta) \cdot Y(m - T_{win}f_p(\delta)) + V_p(\delta) \cdot Y(m + T_{win}f_p(\delta))] \quad (16)$$

where $\bar{V}_p(\delta) = (l_p(\delta)/2j) e^{j\phi_p(\delta)}$, $V_p(\delta)$ its complex conjugate and $Y(m) = -0.25v(m-1) + 0.5v(m) - 0.25v(m+1)$ being the Fourier transform of the Hanning window, where

$$v(m) = e^{-jm\pi(D-1)/D} \cdot \frac{\sin(m\pi)}{\sin(m\pi/D)} \quad (17)$$

Finally, substituting (13) in (16) can lead to an improved δ , namely,

$$\tilde{\delta} = \psi \frac{2|\tilde{L}_p(m_1 + \psi)| - |\tilde{L}_p(m_1)|}{|\tilde{L}_p(m_1 + \psi)| + |\tilde{L}_p(m_1)|} \quad (18)$$

where $\tilde{L}_p(m) = \frac{1}{W} \sum_{d=0}^{D-1} w(d) \cdot \hat{l}_p(d) \cdot e^{-jm\kappa_d} - \frac{1}{W} V_p(\delta) Y(m + m_1 + \delta)$. Thus, the final-e-IPDFT-estimates for nodal-voltage magnitudes, phase-angle and frequency are respectively given by $l_p(\tilde{\delta})$, $\phi_p(\tilde{\delta})$ and $f_p(\tilde{\delta})$.

4.2. Full synchrocheck algorithm

Alg. 2 summarizes the proposed synchrocheck algorithm running on the SYNCHRO block with the refresh-period ΔT_{SYN} . Taking as input samples of the three-phase upstream ($\hat{E}_{up}(d)$) and downstream ($\hat{E}_{down}(d)$) PCC nodal voltages, it computes the magnitude, phase-angles and frequencies of all the signals using the e-IPDFT method presented in Section 4.1 and checks whether, for each phase, the differences between the phasors are within the bounds, i.e. $tol_E = 10\%$, $tol_\phi = 0.34$ rad and $tol_f = 0.3$ Hz, presented in [2]. If all criteria are satisfied, the intra-iteration counter (Count) is updated. If all constraints are satisfied for several subsequent timesteps (i.e. Count is larger or equal than an input parameter n_{syn}), the boolean-flag-output of Alg. 2, i.e. SYNC, is set to 1, otherwise, it is set to 0. Setting SYNC to 1 confirms the synchronization of the inputted three-phase signals which means that the PCC breaker can be securely closed.

Algorithm 2 Proposed synchrocheck

Inputs: Count, $\lambda = 1$, $\hat{E}_{up}(d)$, $\hat{E}_{down}(d)$, $d \in [0, D-1]$

Parameters: n_{syn} , tol_E , tol_ϕ , tol_f

for $j \in \{a, b, c\}$ **do** # Loop for each-phase
 Compute $[E_{up}^j, \phi_{up}^j, f_{up}^j] = \text{eIPDFT}(\hat{E}_{up}^j(d))$
 Compute $[E_{down}^j, \phi_{down}^j, f_{down}^j] = \text{eIPDFT}(\hat{E}_{down}^j(d))$
 Compute $\lambda = \lambda \wedge \left(\left| 1 - \frac{\min\{E_{up}^j, E_{down}^j\}}{\max\{E_{up}^j, E_{down}^j\}} \right| \leq tol_E \right) \wedge$
 $(|\phi_{up}^j - \phi_{down}^j| \leq tol_\phi) \wedge$
 $(|f_{up}^j - f_{down}^j| \leq tol_f)$
end for
if $\lambda == 1$ **then** Count = Count + 1 **else** Count = 0 **end if**
if Count $\geq n_{syn}$ **then** SYNC = 1 **else** SYNC = 0 **end if**

Output: SYNC

5. Experimental validation

5.1. Setup

The experimental validation of the proposed PCC-control and synchrocheck algorithms was done on the EPFL-DESL microgrid [24]. Fig. 3 shows a schematic depiction of the ADN with its base-values. The EPFL-DESL-ADN is a three-phase replica of the CIGRE benchmark microgrid whose description and branch parameters can be found in [25]. The PMUs of the ADN are all streaming measurements to the phasor-data-concentrator of the CMS (unit that runs the state-estimation-process). The agents in Fig. 3 are software-based units that can monitor and explicitly-control the resources they are connected to. Agents also bidirectionally communicate with the ADN-CC through user-datagram-protocol on a wired local-area-network. The synchro-breaker (SB) is composed of a software unit coupled with a controllable circuit-breaker (CCB) – the Compact NSX 250F by Schneider-Electric [26]. The SB runs Alg. 2 and, when it detects that the nodal voltages on both sides of the PCC (i.e. B01 in Fig. 3) are synchronized (i.e. SYNC = 1), it sends an actuation signal that orders the CCB to close. All software-codes (i.e. ADN-CC, SYNCHRO, Agents and CMS) were implemented using LabView on CompactRIOs provided by National Instruments.¹²

5.2. Experimental notes

For the ADC-CC block, due to the relatively low-power rating of the resources in the EPFL-DESL microgrid, the decoupled-gradient-decent method presented in Section 3.4 is used in this paper's experimental-validation. The control-period ΔT and the prediction-horizon ΔT_h of the ADN-CC were set to, respectively, 100 ms and 300 ms. The number of centering-steps n_c , gradient-steps n_g , the reduction parameter μ and the scaling parameter η of Alg. 1 were set to, respectively, 3, 5, 10 and 0.1. As previously stated, the backtracking-line-search algorithm (BLSA) used in Alg. 1 is the one presented in [21, pp. 33–35]. The latter's reduction factor of the step-size, minimum admissible decrease in the objective and maximum number of iterations, are set to, respectively, 0.5, 0.3 and 10. The latter parameters are chosen to ensure that during the BLSA's last iteration the setpoints residues are negligible. Furthermore, in the implemented version of Algo. 1, the alternating-projections method is made more conservative. Indeed, projecting exactly onto a constraint might be problematic since the logarithmic barrier of a binding inequality constraint is undefined. Therefore, numerical issues

¹² More details about the hardware and software infrastructures of the EPFL-DESL microgrid can be found in [24].

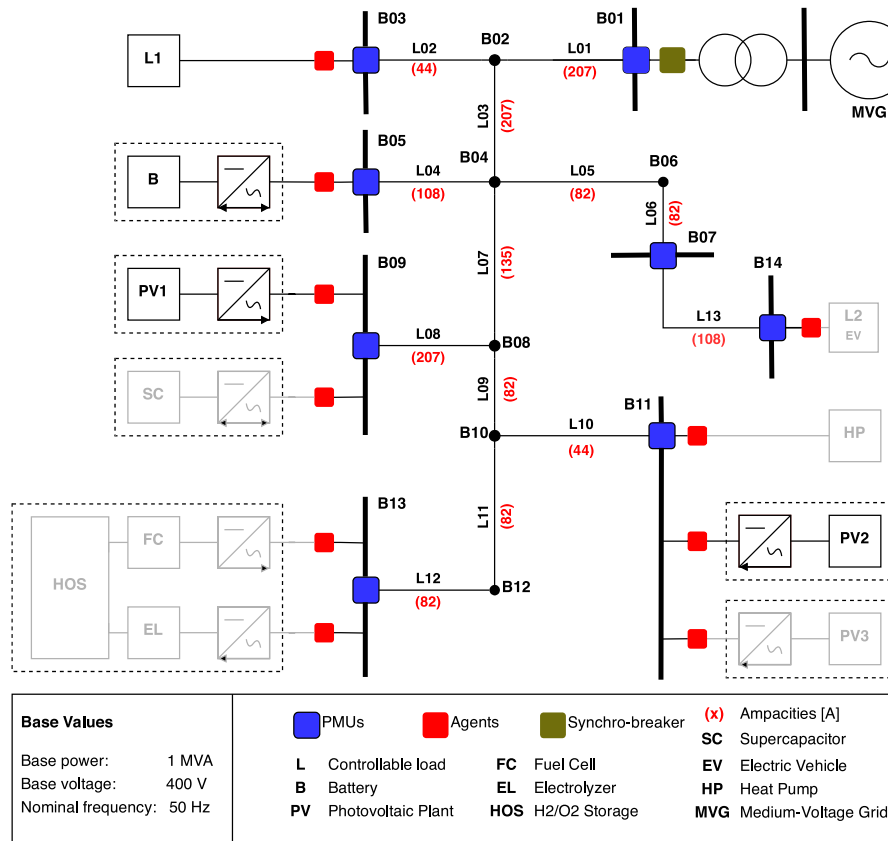


Fig. 3. EPFL-DESL microgrid schematic diagram. Greyed-out resources were not used in the experiment of Section 5.3.

are avoided by projecting onto constraints with a margin of 1% inwards the feasibility regions of said constraints.

For the SYNCHRO block, a refresh period T_{SYN} of 50 ms is chosen and the number of successive positive tolerances check to declare synchronization n_{syn} is set to 20.

Finally, in its present form, the EPFL-DESL microgrid is practically a balanced three-phase grid. As a result, in the ADC-CC block the unbalanced constraints (6f)–(6g) are always verified. Consequently, in the next section, only the values of nodal-voltages and branch-currents of phase a of the microgrid are shown.

5.3. Results

The experimental validation performed in this paper consists of running both the ADN-CC and SYNCHRO blocks on the microgrid depicted in Fig. 3. The microgrid starts in islanded-mode with a 5 kVA/25 kWh battery acting as its slack (i.e. CPC in grid-forming-mode), two controllable (i.e. CPCs in grid-following-mode) resources, namely, a balanced-three-phase controllable load (L1) and PV plant (PV1) with, respectively, 25 kW/25 kVar and 4 kW¹³/10 kVar peak powers, and a non-controllable resource in the form of a PV plant (PV2) with 3 kW¹³/0 kVar peak powers. In order, to stress-test the developed PCC-control algorithm tight operational bounds were chosen, namely, $E_{i,min} = [1, 1, 1]$ p.u., $E_{i,max} = [1.05, 1.05, 1.05]$ p.u. $\forall i \in \mathcal{N} \setminus \mathcal{S}$ and $I_{ij,max} = [10, 10, 10]$ A, $\forall (i, j) \in \mathcal{L}$. Furthermore, the initial grid-state is deliberately chosen outside the feasibility set Γ (i.e. violates grid-operational and resource (see *lim* in Figs. 4 to 6) constraints).

The results of the experiment are shown in Figs. 4 to 6. At $t = 1$ s the resynchronization process (i.e. ADN-CC) is activated. In a

few iterations (~ 300 ms) the grid is forced into the feasibility set as shown in Figs. 5 & 6. Simultaneously, the realignment of the PCC nodal-voltage phasors is pursued and is achieved at $t = 2.5$ s, i.e. 1.5 s after the beginning of the resynchronization process. The alignment is guaranteed for the rest of the simulation as seen by the green-rectangles in Fig. 4. Fig. 4 shows that the proposed synchrocheck detects synchronization exactly 1 s after the criteria were met. This is perfectly in-line with our design choice as the SYNCHRO block's refresh period is set to 50 ms and the number of positive-successive-tolerances checks needed for it to detect synchronism is set to 20, i.e. synchronization should be detected after 1 s of successive tolerance checks. To further benchmark our method, Fig. 4 shows that the Micom P143 relay [14] (Schneider SYNCHRO) also detects synchronism at $t = 2.5$ s. It is important to note that, the Micom P143's synchronism check relies on the three-phase balanceness of the upstream-grid and only senses phase- a of the nodal voltage signal of the upstream grid. The developed synchrocheck *does not* rely on such assumption and is therefore more robust against upstream-grid-irregularities. Finally, it can be seen that some resource injections (and consequently some branch-currents) keep oscillating after the synchronization (i.e. after the 2.5 s mark), this is due to the gradient-descent-nature of the proposed PCC-control process that is naturally oscillating around a *feasible* equilibrium. Such oscillations can be reduced through the tuning of the parameters of Alg. 1 (e.g. re-tuning the BLSA parameters, the scaling parameter and/or the reduction parameter).

6. Conclusion

This paper proposed: (i) a centralized PCC-control in the form of an algorithm that approximately solves an OPF aiming to steer an ADN's downstream PCC nodal voltages towards their upstream counterparts while guaranteeing three-phase-unbalanced operational, i.e. static and

¹³ The low active peak power of the PV plants was due to the fact that experiments were held on a cloudy day.

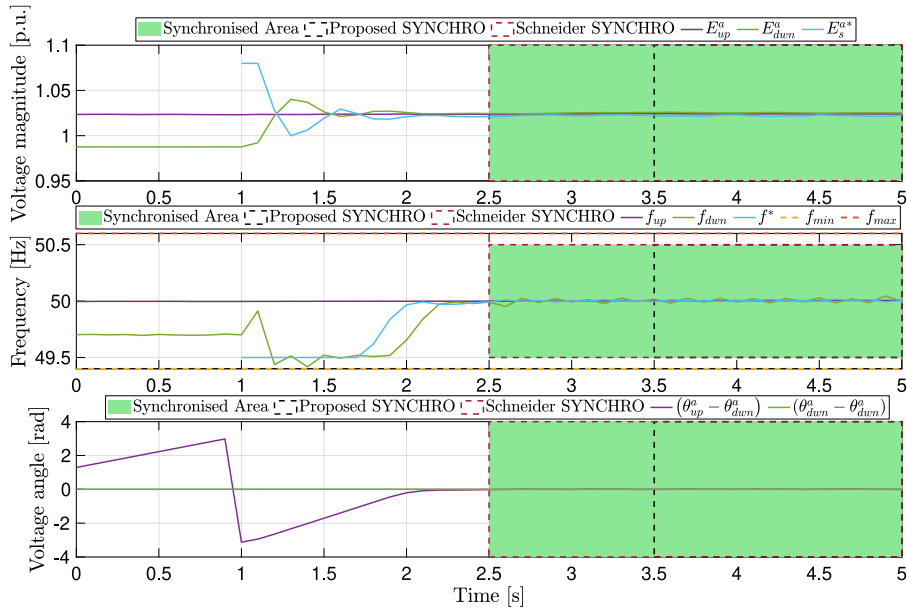


Fig. 4. PCC voltage magnitudes, phase-angles and frequency.

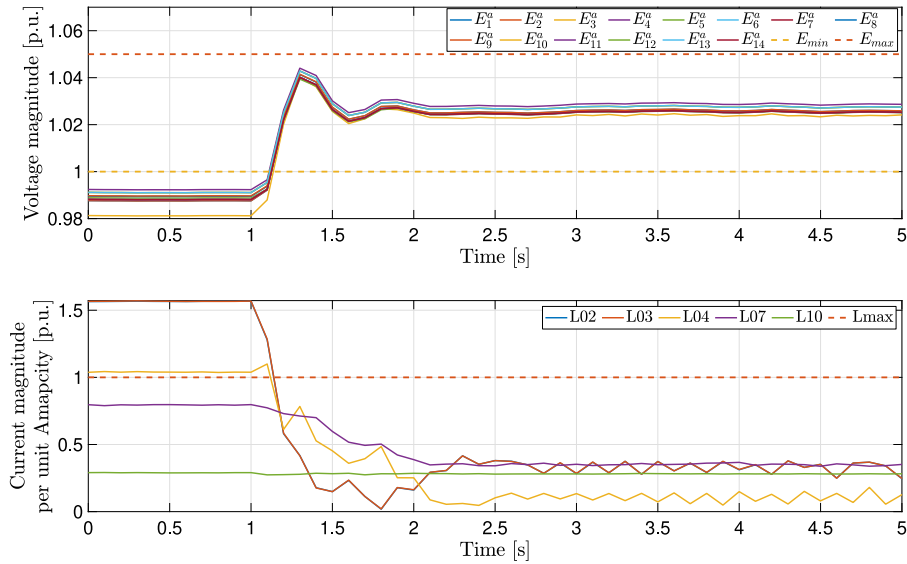


Fig. 5. Voltage and branch current magnitudes — Phase a.

power-quality, constraints for the ADN, and (ii) a synchrocheck algorithm relying on e-IpDFT phasor extraction to determine whether two three-phase phasors are aligned or not. Both contributions were experimentally validated on the EPFL-DESL microgrid. The proposed synchrocheck was further benchmarked against a Micom P143 grid-relay with synchronism check provided by Schneider Electric [14]. Unlike the proposed methods, the Micom P143 is designed to *only* detect, i.e. no resource control, synchronization and relies on the assumption that the PCC upstream nodal voltages are perfectly balanced. The experimental validation showed that within 1.5 s the resynchronization of PCC nodal-voltages was achieved by the proposed algorithm even if the process was launched when the islanded-microgrid was in an infeasible state. Finally, due to its present configuration, the tested microgrid was operating in a balanced three-phase condition which lacked in showcasing the ability of the proposed PCC-control algorithm to deal with unbalances. As a result, following planned three-phase control-enabling-expansions of the EPFL-DESL microgrid, further

experimental validations will be carried out to showcase the ability to *securely* resynchronize an ADN to its upstream grid while not only guaranteeing static but also power-quality operational constraints.

CRedit authorship contribution statement

Sherif Fahmy: Conceptualization, Methodology, Data curation, Writing – original draft, Writing – review & editing, Visualization, Supervision, Project administration. **Quentin Walger:** Conceptualization, Methodology, Software, Writing – original draft. **Mario Paolone:** Conceptualization, Methodology, Writing – review & editing, Supervision.

Declaration of competing interest

The authors declare that they have no known competing financial interests or personal relationships that could have appeared to influence the work reported in this paper.

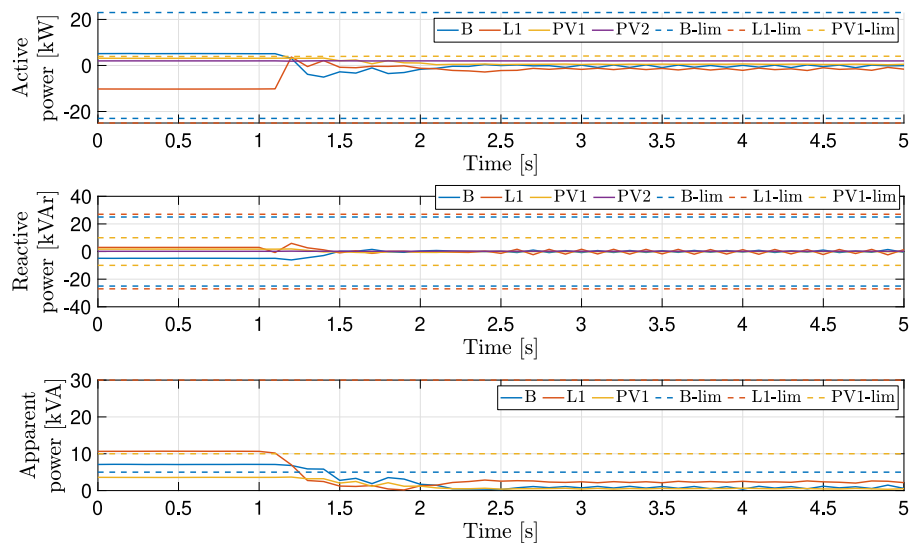


Fig. 6. Three-phase resources' nodal power injections.

References

- [1] IEEE Guide for Design, Operation, and Integration of Distributed Resource Island Systems with Electric Power Systems, IEEE Std 1547.4-2011, 2011, pp. 1–54.
- [2] IEEE Standard for Interconnecting Distributed Resources with Electric Power Systems, IEEE Std 1547-2003, 2003, pp. 1–28.
- [3] IEEE Power System Relaying Committee et al., IEEE Guide for Automatic Reclosing of Line Circuit Breakers for AC Distribution and Transmission Lines, IEEE Power Engineering Society, USA, 2003.
- [4] D. Shi, Y. Luo, R.K. Sharma, Active synchronization control for microgrid reconnection after islanding, in: IEEE PES Innovative Smart Grid Technologies, Europe, IEEE, 2014, pp. 1–6.
- [5] T. Uten, C. Charoenlarnnoppapart, P. Suksompong, Synchronization control for microgrid seamless reconnection, in: 2019 14th International Joint Symposium on Artificial Intelligence and Natural Language Processing (ISAI-NLP), IEEE, 2019, pp. 1–6.
- [6] M.Y. Worku, M.A. Hassan, M.A. Abido, Power management, voltage control and grid synchronization of microgrids in real time, Arab. J. Sci. Eng. 46 (2) (2021) 1411–1429.
- [7] C. Cho, J.-H. Jeon, J.-Y. Kim, S. Kwon, K. Park, S. Kim, Active synchronizing control of a microgrid, IEEE Trans. Power Electron. 26 (12) (2011) 3707–3719.
- [8] F. Tang, J.M. Guerrero, J.C. Vasquez, D. Wu, L. Meng, Distributed active synchronization strategy for microgrid seamless reconnection to the grid under unbalance and harmonic distortion, IEEE Trans. Smart Grid 6 (6) (2015) 2757–2769.
- [9] D. Shi, X. Chen, Z. Wang, X. Zhang, Z. Yu, X. Wang, D. Bian, A distributed cooperative control framework for synchronized reconnection of a multi-bus microgrid, IEEE Trans. Smart Grid 9 (6) (2017) 6646–6655.
- [10] T. Xu, J. Zhou, H. Yang, P. Li, L. Yu, X. Guo, Consensus based distributed angle droop control for islands resynchronization, in: 2020 IEEE Power & Energy Society General Meeting (PESGM), IEEE, 2020, pp. 1–5.
- [11] A. Peiravi, Design and prototyping of a microcontroller based synchrocheck relay for improved reliability, J. Am. Sci. 5 (2009).
- [12] C. Lassetter, E. Cotilla-Sanchez, J. Kim, A learning scheme for microgrid reconnection, IEEE Trans. Power Syst. 33 (1) (2017) 691–700.
- [13] R. Abd Allah, Correlation-based synchro-check relay for power systems, IET Gener. Transm. Distrib. 12 (5) (2018) 1109–1120.
- [14] Easergy MiCOM P14x, 2021, shorturl.at/csYZ9, Accessed last: 2021-09-29.
- [15] IEEE Standard for the Specification of Microgrid Controllers, IEEE Std 2030.7-2017, 2018, pp. 1–43.
- [16] H. Jiayi, J. Chuanwen, X. Rong, A review on distributed energy resources and MicroGrid, Renew. Sustain. Energy Rev. 12 (2008) 2472–2483.
- [17] S. Fahmy, M. Paolone, Analytical computation of power grids' sensitivity coefficients with voltage-dependent injections, in: 2021 IEEE Madrid PowerTech, IEEE, 2021, pp. 1–6.
- [18] A.M. Kettner, M. Paolone, On the properties of the power systems nodal admittance matrix, IEEE Trans. Power Syst. 33 (1) (2018) 1130–1131.
- [19] A. Ortega, F. Milano, Estimation of voltage dependent load models through power and frequency measurements, IEEE Trans. Power Syst. (2020) 1.
- [20] EN Standard, 50160, in: Voltage Characteristics of Public Distribution Systems, Vol. 18, 2010.
- [21] S. Boyd, L. Vandenberghe, Convex Optimization, Cambridge University Press, 2004.
- [22] S. Agmon, The relaxation method for linear inequalities, Canad. J. Math. 6 (1954) 382–392.
- [23] P. Romano, M. Paolone, Enhanced interpolated-DFT for synchrophasor estimation in FPGAs: Theory, implementation, and validation of a PMU prototype, IEEE Trans. Instrum. Meas. 63 (12) (2014) 2824–2836.
- [24] L. Reyes-Chamorro, A. Bernstein, N.J. Bouman, E. Scolaro, A.M. Kettner, B. Cathiard, J.-Y. Le Boudec, M. Paolone, Experimental validation of an explicit power-flow primary control in microgrids, IEEE Trans. Ind. Inf. 14 (11) (2018) 4779–4791.
- [25] S. Papanthanasassiou, N. Hatzigiargyriou, K. Strunz, et al., A benchmark low voltage microgrid network, in: Proceedings of the CIGRE Symposium: Power Systems with Dispersed Generation, CIGRE, 2005, pp. 1–8.
- [26] NSX250F micrologic 2.2 250a 4P4D, 2021, shorturl.at/hzCKS, Accessed last: 2021-09-29.